Sánchez Tovar, R.; Fernández Domene, RM.; García-García, D.; García Antón, J. (2015). Enhancement of photoelectrochemical activity for water splitting by controlling hydrodynamic conditions on titanium anodization. Journal of Power Sources. 286:224-231. doi:10.1016/j.jpowsour.2015.03.174.

ENHANCEMENT OF PHOTOELECTROCHEMICAL ACTIVITY FOR WATER SPLITTING BY CONTROLLING HYDRODYNAMIC CONDITIONS ON TI ANODIZATION

Sánchez-Tovar, R.; Fernández-Domene, R.M., García-García, D.M., García-Antón, J. *

Ingeniería Electroquímica y Corrosión (IEC). Departamento de Ingeniería Química y Nuclear. ETSI Industriales. Universitat Politècnica de València. Camino de Vera s/n, 46022 Valencia, Spain.

Tel. 34-96-387 76 32, Fax. 34-96-387 76 39, e-mail: jgarciaa@iqn.upv.es

This work studies the electrochemical and photoelectrochemical properties of a new type of TiO_2 nanostructure (nanosponge) obtained by means of anodization in a glycerol/water/NH_4F electrolyte under controlled hydrodynamic conditions. For this purpose different techniques such as Scanning Electronic Microscopy (SEM), Raman Spectroscopy, Electrochemical Impedance Spectroscopy (EIS) measurements, Mott-Schottky (M-S) analysis and photoelectrochemical water splitting tests under standard AM 1.5 conditions have been carried out. Obtained results have shown that electron-hole separation is facilitated in the TiO_2 nanosponge if compared with highly ordered TiO_2 nanotube arrays. As a result, nanosponges enhance the photoelectrochemical activity for water splitting.

Keywords: TiO_2 nanostructures, anodization, hydrodynamic conditions, water splitting, Electrochemical Impedance Spectroscopy, Mott-Schottky analysis.

1. INTRODUCTION

Titanium dioxide (TiO_2) is widely used as a pigment, as a catalyst support and as a photocatalyst, among others 1. This last application has attracted a great scientific and technological interest over the last years [1-38] due to the exclusive set of properties of TiO_2, such as a high chemical stability, resistance to photocorrosion and favourable band-edge position relative to the redox potentials for the decomposition of water, allowing for effective direct water splitting using light.

TiO_2 is habitually used in form of nanostructures, such as nanoparticles [24, 30, 37], nanorods/nanowires [20, 26, 37] or nanotubes [1, 6-9, 13-15, 17-19, 22-36, 38], to obtain high specific surfaces areas and, thus, to increase the photocatalytic activity. In the last years, TiO_2 nanotubes have gained increasing attention since they have several advantages with respect to other nanostructures due to their perfectly defined geometry (highly ordered nanotube arrays and a very precise control of their dimensions using the process of anodization for their synthesis) [1]. Furthermore, as the oxide nanotubes formed by anodization are grown directly on the metal substrate (back contact), they can be used directly as photoanodes, thus avoiding compaction or sintering of TiO_2 nanoparticles on the metallic substrate.

In recent publications, the influence of hydrodynamic conditions on the anodization process has been evaluated [31], and it has been observed that under flux conditions the geometry of the formed nanostructures is different from that obtained under stagnant conditions, i.e., nanotubes. This new nanostructure, called nanosponge, provides better performance than tube morphologies, for example, for the water splitting process [31].

In the present work, TiO_2 nanotubes and nanosponges have been obtained by anodization in a glicerol/water/NH_4F mixture using different hydrodynamic conditions. The morphology and electronic properties of both nanostructures have been studied through different techniques, such as Scanning Electronic Microscopy (SEM), Raman Spectroscopy, Electrochemical Impedance Spectroscopy (EIS) measurements and Mott-Schottky (M-S) analysis. These properties have been correlated to the performance of both nanostructures as photocatalysts for water splitting.

2. MATERIALS AND METHODS

Anodization under hydrodynamic conditions was performed in a 2-electrode electrochemical cell with a rotating electrode configuration. The anode was a Teflon coated titanium rod (8 mm diameter, 99.3% purity) in a rotating electrode setup. For all experiments, 0.5 cm^2 of the sample was exposed to the electrolyte. Prior to the anodization process, the titanium rod surface was abraded with 500 to 4000 silicon carbide (SiC) papers, in order to obtain a mirror finish. After this, the sample was sonicated in ethanol for 2 min and dried in a N_2 stream. For anodization a voltage source was used, where the titanium rod served as working electrode and a platinum mesh acted as counter electrode. The electrolyte for these experiments was a mixture of glycerol/water/ammonium fluorine at a concentration of 0.27 M NH_4F in glycerol/water (60:40 vol.%). Different rotation speeds were used: 0, 654, 1307, 1961 and 2614 rpm corresponding to Reynolds numbers (Re) of 0, 100, 200, 300 and 400. The Reynolds numbers (Re) were calculated as follows:

$$\mathrm{Re} = \frac{\omega \cdot r^2 \cdot \rho}{\mu} \qquad \textbf{(1)}$$

where ω is the rotation speed expressed in rad s^{-1}, r is the radius of the working electrode in cm and ρ and μ are the density in g cm^{-3} and dynamic viscosity in g cm^{-1} s^{-1} of the solution, respectively [39].

The specimens were anodized at 30 V by increasing the potential from zero to the desired value at a rate of 200 mV s^{-1}, followed by keeping the end potential for 3 hours. To compare the electrochemical and photoelectrochemical behavior of TiO_2 nanostructures with that of a compact TiO_2 layer, this layer was obtained anodizing the titanium rod in the same electrochemical cell, i.e., using platinum as counter electrode in 1M H_2SO_4 at 30 V for 20 min under stagnant conditions.

After each test, a field-emission scanning electron microscope (FE-SEM) was used for morphological characterization of the obtained samples. For electrochemical (EIS and M–S measurements) and photoelectrochemical water splitting measurements, the asformed TiO_2 layers were annealed in a furnace at 450 °C (heating at 30 ºC s^{-1}) in air for 1 h. The materials were also examined by Raman spectroscopy ("Witec Raman microscope") after the heat treatment, in order to evaluate their crystalline structure. For these measurements, a 632 nm neon laser with 420 μW was used.

For the electrochemical and photoelectrochemical water splitting tests, a three-electrode configuration was used. The area of the TiO_2 nanostructures (working electrode) exposed to the test solution was 0.13 cm^2. A saturated Ag/AgCl (3 M KCl) electrode was the reference electrode, and a platinum tip was the counter electrode.

The electrochemical measurements were conducted in a 0.1 Na_2SO_4 solution using an Autolab PGSTAT302N potentiostat under dark conditions (without irradiation). EIS experiments were conducted at the open circuit potential (OCP) over a frequency range from 100 kHz to 10 mHz with a 10 mV (peak to peak) signal amplitude. Mott–Schottky plots were subsequently obtained by sweeping the potential from the OCP in the negative direction at 10 mV s^{-1} with an amplitude signal of 10 mV at a frequency value of 10 kHz.

The photoelectrochemical experiments were carried out under simulated sunlight condition AM 1.5 (100 mW cm^2) in a 1M KOH solution. Photocurrent vs. voltage characteristics were recorded by scanning the potential from −0.8 V to +0.5 V with a scan rate of 2 mV s^{-1}. Photocurrent transients as a function of the applied potential were recorded by chopped light irradiation (60 s in the dark and 20 s in the light). Samples were left at +0.5 V in the light for one hour, in order to evaluate their stability to the photocorrosion attack.

3. RESULTS AND DISCUSSION

Figure 1 shows the scanning electron microscope (SEM) images of the TiO_2 nanostructures obtained under stagnant conditions (Re = 0, **Figure 1a**) and under hydrodynamic conditions (Re = 300, **Figure 1b**). Under stagnant conditions, organized nanotubes of 1.3 μm in length with pore diameters of 130 and 224 nm in inner and outer diameter were formed. On the other hand, the hydrodynamic conditions changed the morphology of the formed nanostructures from nanotubes to nanosponges, i.e., a connected and highly porous TiO_2 structure. **Figure 2** shows that the thickness of the

nanosponges is enhanced in comparison to that obtained for the nanotubes. Additionally, an increase in the rotation rate made nanosponges thicker (from 2 to nearly 3.5 μm). The formed nanosponges have pore openings of roughly 50 nm.

3.2. Raman Spectra

As an example, **Figure 3** shows the spectra of as-prepared and annealed TiO_2 nanostructures for Re = 0 and Re = 300. Raman peaks originate from the molecular bond and provide useful information such as crystal structure, phase purity and crystallinity. The as-prepared TiO_2 does not clearly show defined peaks and only a single baseline is present. According to other studies [40, 41], there are six active RS bands for anatase, i.e.: 144 cm^{-1} (E_g), 197 cm^{-1} (E_g), 399 cm^{-1} (B_{1g}), 513 cm^{-1} (A_{1g}), 519 (B_{1g}) and 639 (E_g). For species after annealing, the specific bands were recorded in the range of 149 cm^{-1}, 197 cm^{-1}, 398 cm^{-1}, 516 cm^{-1}, 637 cm^{-1}. These results show that the heat treatment improves the crystallinity of TiO_2 and the peaks obtained correspond to TiO_2 anatase phase.

3.3. EIS measurements

Figure 4 shows the experimental Nyquist and Bode plots for the compact TiO_2 film and TiO_2 nanostructures formed at different Re, measured in a 0.1M Na_2SO_4 solution at open circuit potential under dark conditions and at 25º C. In the case of the compact TiO_2 film, Nyquist and Bode plots exhibit the typical passive state behavior characterized by a semicircular shape and high impedance values in the Nyquist and Bode-module plots (**Figures 4(a) and 4(d))**, as well as phase angles close to 90 degrees (**Figure 4(c))**, suggesting the formation of a highly stable TiO_2 passive film on the Ti

electrode [42]. The presence of a shoulder in the Bode-phase plot at intermediate frequencies (**Figure 4(c))** suggests the existence of two time constants.

In the case of the TiO_2 nanostructures (nanotubes and nanosponges), the presence of two well-defined time constants can be observed, which could be associated with the nanoporous nature of the TiO_2 layer [27]. The shape of the EIS plots is characterized in this case by a distorted small semicircle at high frequencies followed by an unfinished semicircle at low frequencies, with a much higher amplitude (**Figures 4(b) and 4(c))**. In this case, impedance values are clearly lower than for the compact TiO_2 film (**Figures 4(a) and 4(d)**). It can be observed from the inset in **Figure 4(b)** that the amplitude of the small semicircle at high frequencies is larger for Re = 0 and decreases with increasing Re values. Furthermore, two peaks are perfectly discernible from Bode-phase plots, the peak at low frequencies being always higher than that at high frequencies, regardless of the value of Re.

Experimental EIS data can be represented with an electrical equivalent circuit made up of two RC time constants associated in series (**Figure 5**). This equivalent circuit has been used in the literature to model the impedance data of compact and nanoporous TiO_2 films [7, 8, 14, 27, 34, 43]. Constant phase elements (CPEs) have been used instead of pure capacitors to account for frequency dispersion and non-ideality. CPEs have been converted into pure capacitances, *C*, by using the following equation [44, 45]:

$$C = \frac{(Q \cdot R)^{1/\alpha}}{R} \qquad \textbf{(2)}$$

where Q is the impedance of the CPE and R corresponds to R_2 when determining capacitance values of the second time constant in **Figure 5**. To determine C_1 from CPE_1, R has been calculated as follows:

$$\frac{1}{R} = \frac{1}{R_S} + \frac{1}{R_1} \quad \textbf{(3)}$$

The values of the equivalent circuit parameters are shown in **Table 1**, where R_S is always the electrolyte resistance. In the case of the compact TiO_2 film the time constant at high frequencies (R_1CPE_1) is related to the outer layer of the passive film, and the low-frequency behavior is attributed to the inner layer of the film, more compact than the outer one [42, 43]. In the case of the nanostructured TiO_2 layers, and according to the obtained values, the R_1CPE_1 time constant is related to the TiO_2 nanoporous structure [5, 14, 22], whereas the R_2CPE_2 time constant is associated with the charge transfer processes at the bottom of the TiO_2 layer [5, 14] or with a compact TiO_2 underlayer [7, 8, 22].

The values of R_1 and R_2 for the compact TiO_2 film are of the order of hundreds of $k\Omega\ cm^2$ (**Table 1**). In the case of the nanostructures, it can be observed that R_2 values are similar to those obtained for the compact TiO_2 film and are significantly higher (two orders of magnitude) than the values associated with the internal resistance of the nanostructures, R_1. These results imply, first, that in the case of the TiO_2 nanostructures R_2 can be associated with a compact TiO_2 underlayer; second, that the nanoporous overlayer (TiO_2 nanotubes and nanosponges) has a higher surface area and higher density of defects than the compact TiO_2 underlayer, leading to a higher conductivity compared to the base oxide [22, 27].

The CPE_1 constant, α_1, takes values of 0.7-0.8 and is always lower than α_2, the latter being close to unity in all cases. These results imply a significantly rough morphology of the nanoporous TiO_2 overlayer (nanotubes and nanosponges), more conductive and defective than the underlying TiO_2 layer whose behavior approximates that of an ideal capacitor [27, 34]. For the nanoporous structures, C_1 values are considerably lower than those of C_2, regardless of the value of Re. Besides, C_2 values are visibly higher in the case of the nanostructures than for the compact TiO_2 film. The high values obtained for C_2 can be explained by a decrease in the TiO_2 underlayer thickness or by an increase in the porosity of this layer as a consequence of a transition from a mostly compact inner layer to a porous layer [7, 27].

Concerning the comparison between the different nanostructures obtained in this work (nanotubes and nanosponges), the resistance of these nanostructures, R_1, decreases with increasing Re, indicating that the nanosponges formed under hydrodynamic conditions possess higher electrical conductivity than the nanotubes formed under stagnant conditions. No clear tendency of R_2 values is observed with Re, indicating that the electrical properties of the compact TiO_2 underlayer are not dependant on the hydrodynamic conditions. Together with the lower values of α_1 in the case of $Re > 0$, the previous results indicate a higher degree of porosity in the nanosponges formed under hydrodynamic conditions compared with the nanotubes formed with $Re = 0$. The decrease in C_1 with increasing Re can be explained by a decrease in the density of charge carriers in the nanosponges [35], as it will be verified later with Mott-Schottky analysis.

3.4. Mott-Schottky analysis

Figure 6(a) shows the Mott-Schottky plots at a frequency of 10 kHz for the compact TiO_2 film and TiO_2 nanostructures formed at different Re, measured in a 0.1M Na_2SO_4 solution at open circuit potential under dark conditions and at 25º C. These plots have been obtained at a frequency of 10 kHz since at this high value the capacitance dependence on frequency is eliminated [16, 42, 46]. **Figure 6(b)** is a magnification and only shows the M-S plots for the TiO_2 nanostructures. The positive slopes of the M-S plots are characteristics of *n*-type semiconductors, with the dominant defects in TiO_2 being oxygen vacancies due to their lower formation energy compared with Ti^{3+} interstitials [22, 38, 47-51]. It can be observed that capacitance values are notably lower for the compact TiO_2 layer (higher values of C^{-2}), which is consistent with capacitance values obtained above by EIS (**Table 1**).

The donor density, N_D, can be determined from the positive slopes of the straight lines in the M-S plots using the Mott-Schottky equation for an *n*-type semiconductor. Although the M-S equations were derived based on a flat electrode, this analysis has been widely used to irregular geometries with porous surfaces such as nanostructures [7, 8, 22, 25, 27, 30, 37, 38, 46, 52]. Hence, a qualitative comparison between N_D values obtained for different TiO_2 layers and nanostructures is valid. The M-S expression for N_D is [42, 47, 53]:

$$N_D = \frac{2}{\varepsilon\varepsilon_0 e\sigma} \qquad \textbf{(4)}$$

where ε is the dielectric constant of the TiO_2 layers (a value of 60 has been assumed for the compact TiO_2 film [49] and a value of 100 for the TiO_2 nanostructures [34, 38]), ε_0 is the vacuum permittivity ($8.85 \cdot 10^{-14}$ F/cm), e is the electron charge ($1.60 \cdot 10^{-19}$ C) and σ is the positive slope of each straight line in the M-S plots.

The N_D values have been calculated using the geometric area of the electrodes and are presented in **Table 2**. It can be observed that N_D is of the order of 1×10^{18} cm^{-3} for the compact TiO_2 film, while the values for the different nanostructures are considerably higher, of the order of $1\text{-}4 \times 10^{19}$ cm^{-3}. The increase in oxygen vacancies density should improve the *n*-type character of the TiO_2 nanostructures and thus enhance the electron transport along the nanostructures [22, 30, 37].

On the other hand, in the case of the TiO_2 nanostructures, N_D decreases with increasing Re, that is, N_D is lower for the nanosponges than for the nanotubes. Although the increase in N_D can be a positive effect, since this fact increases the electrical conductivity of TiO_2, an increase in N_D can also lead to a decrease in the depletion layer thickness, resulting in an increase of recombination losses [4, 16, 54]. If the depletion layer is very thin, photons can penetrate beyond this layer and light will be absorbed in the bulk semiconductor, where the electrical field is absent [4, 16, 54, 55]. The lack of an electrical field prevents the photo-excited electron-hole pairs from being effectively separated, thus increasing the probability of recombination [4, 16, 27, 54]. Furthermore, oxygen vacancies in TiO_2 have been found to act as recombination centers for electron and holes, playing a critical role in the trapping process: an excess of oxygen vacancies will result in more photogenerated electrons being trapped thus decreasing their contribution to the photoelectrochemical processes [37, 56, 57].

The recombination probability is also affected by the flat-band potential, ϕ_{FB}, which is the potential that needs to be applied to the semiconductor to reduce the band bending to zero, that is, at this potential there is no depleted space charge layer. The ϕ_{FB} value is related to the potential drop at the depletion space charge layer, ϕ_{SC}, and the applied external potential, ϕ_A, according to:

$$\phi_{SC} = \phi_A - \phi_{FB} \quad \textbf{(5)}$$

Assuming a constant value of ϕ_A, the higher and more negative the value of ϕ_{FB}, the higher the value of ϕ_{SC} and, consequently, the stronger the electrical field within the depleted space charge layer, which is the driving force to separate the photogenerated electron-hole pairs. Therefore, to reduce the recombination probability ϕ_{FB} should be high and negative [16, 37].

Values of ϕ_{FB} can be determined from the intercept of the straight line in M-S plots with the potential axis. These values for the compact TiO_2 film and for the different nanostructures are also shown in **Table 2**. It can be observed that ϕ_{FB} is more negative for the compact TiO_2 film, which indicates that the recombination probability is lower than for the TiO_2 nanostructures. However, the low values of N_D in the compact film reduce considerably its photoelectrochemical performance, as it will be demonstrated later. On the other hand, ϕ_{FB} becomes more negative with increasing Re, that is, nanosponges formed under hydrodynamic conditions possess more negative values of ϕ_{FB} than nanotubes formed under stagnant conditions. This negative shift of ϕ_{FB} leads to a displacement of the Fermi level towards the conduction band edge and, consequently, to a larger band bending and electrical field within the depleted space charge layer [22,

26, 37]. Therefore, from the point of view of the charge recombination probability, these results indicate that this probability is lower in the case of the nanosponges.

3.5. Photoelectrochemical water splitting measurements

Figure 7 shows the photoelectrochemical water splitting performance under simulated sunlight AM 1.5 conditions for the different nanostructures. It can be observed in terms of the photocurrent transient vs. potential curves, that the nanostructures obtained under hydrodynamic conditions, present a higher performance in comparison with the nanotubes (anodized at the same potential, time and electrolyte as the nanosponges but at Re = 0) and a significantly higher photoelectrochemical behavior with respect to the compact TiO_2 layer. The high photocurrent density of the nanosponges, especially when Re increases, is directly related to their superior electrical conductivity [14]. These results are in well agreement with the EIS (resistance values) and MS measurements (N_D and ϕ_{FB} values). It is known that a large population of surface-active sites due to the increase in thickness in the nanosponges will lead to the enhanced rate of the photoelectrochemical reaction over the photoelectrode [28, 58]. In order to know if the photocurrent increase was due to the higher thickness of the nanosponges or due to its intrinsic morphology which could proporcionate a high surface area, photocurrent transient vs potential curves were performed for thicker nanotubes (~4 μm, anodized at 55V in ethylenglycol based electrolytes with 2 wt. % of water and 0.1M of NH4F and annealed at 450 ºC). **Figure 8** shows that the photocurrents obtained for the nanotubes are lower than for the thicker nanosponges (obtained at Re = 400). In fact, the photocurrent obtained for the nanotube morphology is lower than the obtained for the

rest of thinner nanosponges. This confirms the suitability of the nanosponge morphology for photocatalysis purposes.

Furthermore, the maximum and minimum for light on and light off shown in **Figure 7** describe two competitive processes, i.e., the former related to the generation of electron-hole pairs at the semiconductor/electrolyte interface and the latter to the recombination of theses pairs [2, 4, 16, 59, 60]. **Figure 7** shows that the initial anodic peak (maximum) is present for all the nanosponges and nanotubes. On the other hand, when the light is switched off, a cathodic peak is observed only for the nanotubes and for the nanosponges synthesised at the lowest Re (Re = 100), due to the recombination of the conduction band electrons with the holes trapped at the surface, consequently decreasing their photocurrent response.

It is remarkable that for both nanotubes and nanosponges, the photocurrent under illumination increases with the applied potential until a potential value of -0.2 V whereas for the compact layer photocurrents remains almost constant from the beginning of the tests. On the other hand, a dark current remains very low in all the studied samples.

Additionally, it is important to highlight that the nanosponges obtained under hydrodynamic conditions do not deteriorate with time. **Figure 9** shows as an example, the photostability in 1 M KOH solution during 1 hour of the different nanostructures holding at 500 mV the potential under AM 1.5 illumination. From **Figure 9** it can be clearly observed that nanosponges synthesized at higher Reynolds numbers are stable with time.

4. CONCLUSIONS

The use of controlled hydrodynamic conditions during titanium anodization generates a TiO_2 interlinked with high surface area morphology (nanosponge morphology).

An increase in N_D has been observed for the TiO_2 nanostructures (nanotubes and nanosponges) compared with the compact TiO_2 layer, which improves the *n*-type character of the nanostructures and enhances electron transport. On the other hand, N_D is lower for the nanosponges than for the nanotubes, which results in thicker depleted layers in the case of the nanosponges that provide a strong electric field essential for a successful separation of photogenerated electrons and holes.

The displacement of the ϕ_{FB} towards more negative values in the case of the nanosponges (with increasing Re) results in an up-shift of Fermi level towards the conduction band and a somewhat larger band bending, which facilitate electron-hole separation.

TiO_2 nanosponges enhance the photoelectrochemical activity for water splitting compared with nanotubes and compact TiO_2 layers, in particular those anodized at higher Reynolds numbers, as a consequence of higher surface areas and a better charge separation.

TiO2 nanosponges synthesized at high Reynolds numbers have been demonstrated to be stable with time.

Acknowledgements: Authors would like to express their gratitude for their financial support to the Generalitat Valenciana (PROMETEOII/2014/009), to Fundación Iberdrola and to the Universitat Politècnica de València.

REFERENCES

[1] J. M. Macak, H. Tsuchiya, A. Ghicov, K. Yasuda, R. Hahn, S. Bauer, P. Schmuki, Curr. Opin. Solid St. Mater. Sci. 11 (2007) 3-18.

[2] A. Hagfeldt, H. Lindström, S. Södergren, S. E. Lindquist, J. Electroanal. Chem. 381 (1995) 39-46.

[3] T. Bak, J. Nowotny, M. Rekas, C. C. Sorrell, Int. J. Hydrogen Energ. 27 (2002) 19-26.

[4] M. Radecka, M. Wierzbicka, S. Komornicki, M. Rekas, Physica B: Condensed Matter 348 (2004) 160-168.

[5] W. H. Leng, Z. Zhang, J. Q. Zhang, C. N. Cao, J. Phys. Chem. B 109 (2005) 15008-15023.

[6] P. Pillai, K. S. Raja, M. Misra, J. Power Sources 161 (2006) 524-530.

[7] A. G. Muñoz, Electrochim. Acta 52 (2007) 4167-4176.

[8] A. G. Muñoz, Q. Chen, P. Schmuki, J. Solid State Electrochem. 11 (2007) 1077-1084.

[9] H. Tsuchiya, J. M. Macak, A. Ghicov, A. S. Räder, L. Taveira, P. Schmuki, Corros. Sci. 49 (2007) 203-210.

[10] S. P. Albu, A. Ghicov, J. M. Macak, R. Hahn, P. Schmuki, Nano Lett. 7 (2007) 1286-1289.

[11] M. Ni, M. K. H. Leung, D. Y. C. Leung, K. Sumathy, Renew. Sust. Energ. Rev. 11 (2007) 401-425.

[12] M. Hepel, I. D. Kumarihamy, Int. J. Hydrogen Energ. 32 (2007) 2693-2702.

[13] S. K. Mohapatra, M. Misra, V. K. Mahajan, K. S. Raja, J. Catal. 246 (2007) 362-369.

[14] P. Xiao, D. Liu, B. Batalla Garcia, S. Sepehri, Y. Zhang, G. Cao, Sensor Actuat. B-Chem. 134 (2008) 367-372.

[15] F. Fabregat-Santiago, E. M. Barea, J. Bisquert, G. K. Mor, K. Shankar, C. A. Grimes, J. Am. Chem. Soc. 130 (2008) 11312-11316.

[16] M. Radecka, M. Rekas, A. Trenczek-Zajac, K. Zakrzewska, J. Power Sources 181 (2008) 46-55.

[17] Z. Liu, B. Pesic, K. S. Raja, R. R. Rangaraju, M. Misra, Int. J. Hydrogen Energ. 34 (2009) 3250-3257.

[18] D. Wang, Y. Liu, B. Yu, F. Zhou, W. Liu, Chem. Mater. 21 (2009) 1198-1206.

[19] T. S. Kang, A. P. Smith, B. E. Taylor, M. F. Durstock, Nano Lett. 9 (2009) 601-606.

[20] A. Wolcott, W. A. Smith, T. R. Kuykendall, Y. Zhao, J. Z. Zhang, Small 5 (2009) 104-111.

[21] M. M. Pedemonte, A. Visintin, A. L. Capparelli, Int. J. Hydrogen Energ. 35 (2010) 6069-6073.

[22] S. Palmas, A. M. Polcaro, J. R. Ruiz, A. Da Pozzo, M. Mascia, A. Vacca, Int. J. Hydrogen Energ. 35 (2010) 6561-6570.

[23] P. Pu, H. Cachet, E. M. M. Sutter, Electrochim. Acta 55 (2010) 5938-5946.

[24] D. D´Elia, C. Beauger, J. F. Hochepied, A. Rigacci, M. H. Berger, N. Keller, V. Keller-Spitzer, Y. Suzuki, J. C. Valmalette, M. Benabdesselam, P. Achard, Int. J. Hydrogen Energ. 36 (2011) 14360-14373.

[25] S. Palmas, A. Da Pozzo, M. Mascia, A. Vacca, A. Ardu, R. Matarrese, I. Nova, Int. J. Hydrogen Energ. 36 (2011) 8894-8901.

[26] G. Wang, H. Wang, Y. Ling, Y. Tang, X. Yang, R. C. Fitzmorris, C. Wang, J. Z. Zhang, Y. Li, Nano Lett. 11 (2011) 3026-3033.

[27] D. P. Oyarzún, R. Córdova, O. E. Linarez Pérez, E. Muñoz, R. Henríquez, M. López Teijelo, H. Gómez, J. Solid State Electrochem. 15 (2011) 2265-2275.

[28] L. x. Sang, Z. Zhi-yu, B. Guang-mei, D. Chun-xu, M. Chong-fang, Int. J. Hydrogen Energ. 37 (2012) 854-859.

[29] S. A. A. Yahia, L. Hamadou, A. Kadri, N. Benbrahim, E. M. M. Sutter, J. Electrochem. Soc. 159 (2012) K83-K92.

[30] L. Yu, Z. Wang, L. Shi, S. Yuan, Y. Zhao, J. Fang, W. Deng, Appl. Catal. B-Environ. 113-114 (2012) 318-325.

[31] R. Sánchez-Tovar, K. Lee, J. García-Antón, P. Schmuki, Electrochem. Commun. 26 (2013) 1-4.

[32] L. Sun, J. Cai, Q. Wu, P. Huang, Y. Su, C. Lin, Electrochim. Acta 108 (2013) 525-531.

[33] P. Acevedo-Peña, I. González, J. Electrochem. Soc. 160 (2013) H452-H458.

[34] L.-K. Tsui, T. Homma, G. Zangari, J. Phys. Chem. C 117 (2013) 6979-6989.

[35] L.-K. Tsui, G. Zangari, Electrochim. Acta 121 (2014) 203-209.

[36] R. G. Freitas, M. A. Santanna, E. C. Pereira, J. Power Sources 251 (2014) 178-186.

[37] D. Wang, X. Zhang, P. Sun, S. Lu, L. Wang, C. Wang, Y. Liu, Electrochim. Acta 130 (2014) 290-295.

[38] L. Aïnouche, L. Hamadou, A. Kadri, N. Benbrahim, D. Bradai, Electrochim. Acta 133 (2014) 597-609.

[39] N. S. Cheng, Ind. Eng. Chem. Res. 47 (2008) 3285-3288.

[40] S. T. Nishanthi, S. Iyyapushpam, B. Sundarakannan, E. Subramanian, D. Pathinettam Padiyan, Sep. Purif. Technol. 131 (2014) 102-107.

[41] X. Zhou, T. Shi, J. Wu, H. Zhou, Appl. Surf. Sci. 287 (2013) 359-368.

[42] R. M. Fernández-Domene, E. Blasco-Tamarit, D. M. García-García, J. García-Antón, J. Electrochem. Soc. 161 (2014) C25-C35.

[43] V. A. Alves, R. Q. Reis, I. C. B. Santos, D. G. Souza, T. d. F. Gonçalves, M. A. Pereira-da-Silva, A. Rossi, L. A. da Silva, Corros. Sci. 51 (2009) 2473-2482.

[44] G. J. Brug, A. L. G. van den Eeden, M. Sluyters-Rehbach, J. H. Sluyters, J. Electroanal. Chem. 176 (1984) 275-295.

[45] B. Hirschorn, M.E. Orazem, B. Tribollet, V. Vivier, I. Frateur, M. Musiani, Electrochim. Acta 55 (2010) 6218-6227.

[46] X. Lu, G. Wang, T. Zhai, M. Yu, J. Gan, Y. Tong, Y. L, Nano Lett. 12 (2012) 1690-1696.

[47] Z. Jiang, X. Dai, H. Middleton, Mater. Chem. Phys. 126 (2011) 859-865.

[48] D. S. Kong, W. H. Lu, Y. Y. Feng, Z. Y. Yu, J. X. Wu, W. J. Fan, H. Y. Liu, J. Electrochem. Soc. 156 (2009) C39-C44.

[49] D. Sazou, K. Saltidou, M. Pagitsas, Electrochim. Acta 76 (2012) 48-61.

[50] B. Roh, D. D. Macdonald, Russ. J. Electrochem. 43 (2007) 125-135.

[51] H. Peng, Phys. Lett. A 372 (2008) 1527-1530.

[52] G. Wang, H. Wang, Y. Ling, Y. Tang, X. Yang, R. C. Fitzmorris, C. Wang, J. Z. Zhang, Y. Li, Nano Lett. 11 (2011) 3026-3033.

[53] A. M. Schmidt, D. S. Azambuja, E. M. A. Martini, Corros. Sci. 48 (2006) 2901-2912.

[54] O. Carp, C. L. Huisman, A. Reller, Prog. Solid State Chem. 32 (2004) 33-177.

[55] U. König, J. W. Schultze, Solid State Ionics 53-56, Part 1 (1992) 255-264.

[56] B. J. Morgan, G. W. Watson, Phys. Rev. B 80 (2009) 233102.

[57] H. Irie, Y. Watanabe, K. Hashimoto, J. Phys. Chem. B 107 (2003) 5483-5486.

[58] J. Gan, X. Lu, T. Zhai, Y. Zhao, S. Xie, Y. Mao, Y. Zhang, Y. Yang, Y. Tong, J. Mater. Chem. 21 (2011) 14685-14692.

[59] D. Tafalla, P. Salvador, R. M. Benito, J. Electrochem. Soc. 137 (1990) 1810-1815.

[60] N. W. Duffy, L. M. Peter, R. M. G. Rajapakse, K. G. U. Wijayantha, Electrochem. Commun. 2 (2000) 658-662.

Tables captions

Table 1. Equivalent circuit parameters for TiO_2 compact layer and TiO_2 nanostructures (nanotubes and nanosponges) at different values of Re.

Table 2. Values of N_D and ϕ_{FB} for TiO_2 compact layer and TiO_2 nanostructures (nanotubes and nanosponges) at different values of Re.

Figures captions

Figure 1. SEM images of the TiO_2 nanostructures (a) under stagnant conditions (Re = 0) and (b) under hydrodynamic conditions (Re > 0).

Figure 2. Length of the nanotubes (Re = 0) and nanosponges (Re > 0) as a function of Re.

Figure 3. Raman spectra of as-prepared and annealed TiO_2 nanostructures for Re = 0 and Re = 300.

Figure 4. Experimental Nyquist (a, b), Bode-phase (c) and Bode-module (d) plots for the compact TiO_2 film and TiO_2 nanostructures formed at different Re values.

Figure 5. Electrical equivalent circuit used to simulate experimental EIS data.

Figure 6. (a) Mott-Schottky plots obtained at a frequency of 10 kHz for the compact TiO_2 film and TiO_2 nanostructures formed at different Re values; (b) magnification of Figure 6(a) showing only the M-S plots for the TiO_2 nanostructures.

Figure 7. Photocurrent transient vs. potential curves for the compact TiO_2 film and TiO_2 nanostructures formed at different Re values under simulated sunlight AM 1.5 illumination.

Figure 8. Photocurrent transient vs. potential curves for ~4 μm nanotubes and ~3.5 μm nanosponges under AM 1.5 illumination.

Figure 9. Photostability experiments carried out in a 1M KOH solution at 500 mV under AM 1.5 illumination.

Table 1

Re	R_S/Ω cm^2	C_1/μF cm^{-2}	α_1	R_1/kΩ cm^2	C_2/μF cm^{-2}	α_2	R_2/kΩ cm^2	χ^2 (x10^{-3})
0	41 ± 4	69 ± 12	0.84 ± 0.05	8.9 ± 2.6	365 ± 63	0.95 ± 0.09	576 ± 42	5
100	36 ± 6	71 ± 10	0.65 ± 0.03	3.6 ± 1.2	434 ± 101	0.98 ± 0.04	289 ± 27	4
200	43 ± 6	40 ± 8	0.68 ± 0.02	2.8 ± 0.5	505 ± 112	0.99 ± 0.01	454 ± 55	2
300	31 ± 7	33 ± 5	0.68 ± 0.07	2.4 ± 0.2	477 ± 116	0.97 ± 0.07	432 ± 104	8
400	31 ± 3	10 ± 2	0.70 ± 0.03	2.1 ± 0.4	902 ± 208	0.89 ± 0.06	860 ± 282	9
COMPACT	39 ± 6	3 ± 1	0.71 ± 0.02	201 ± 23	29 ± 6	0.96 ± 0.04	255 ± 43	0.3

Table 2

Re	N_D **(× 10^{19} cm^{-3})**	ϕ_{FB}**/V vs (Ag/AgCl)**
0	3.6 ± 0.6	-0.15 ± 0.07
100	1.4 ± 0.3	-0.17 ± 0.04
200	1.1 ± 0.1	-0.17 ± 0.02
300	1.1 ± 0.2	-0.21 ± 0.01
400	0.9 ± 0.1	-0.33 ± 0.03
COMPACT	0.17 ± 0.01	-0.55 ± 0.01

Figure 1

Click here to download Figure(s): Figure 1.doc

a) Re = 0

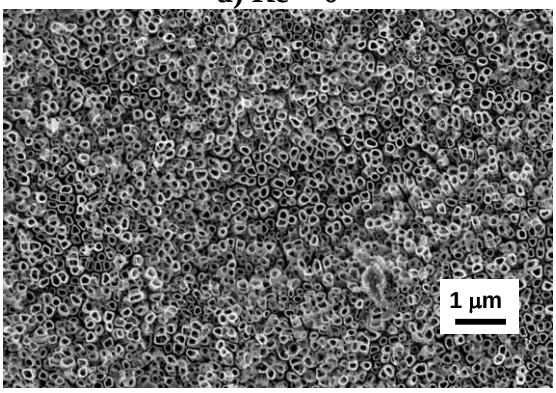

b) Re = 300

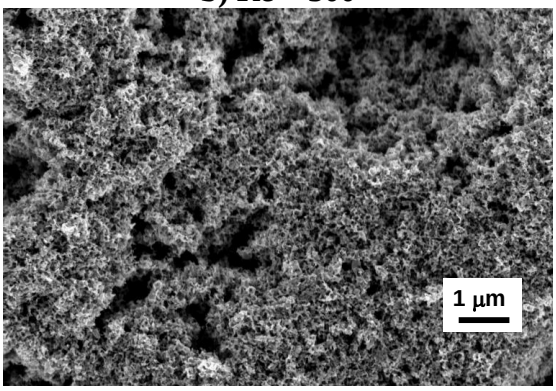

Figure 2

Click here to download Figure(s): Figure 2.doc

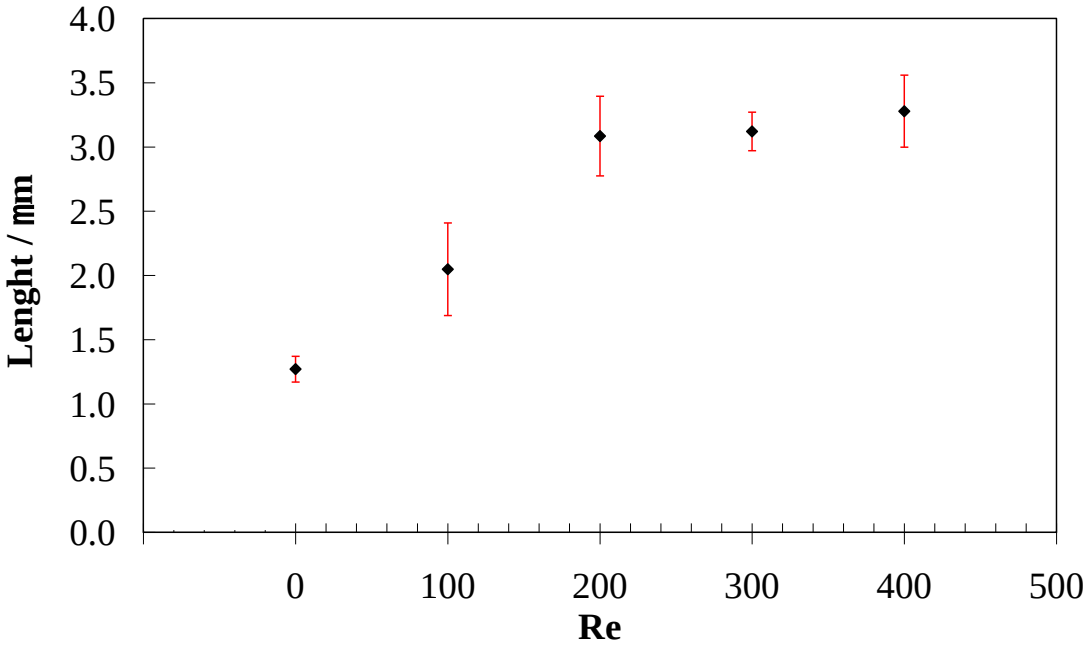

Figure 3

Click here to download Figure(s): Figure 3.doc

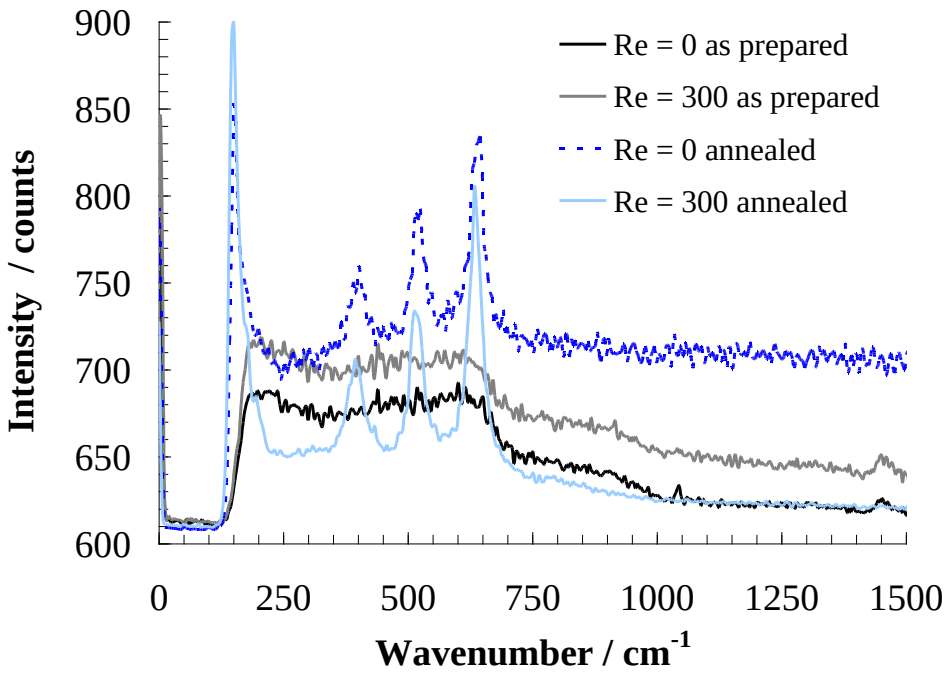

Figure 4

Click here to download Figure(s): Figure 4.doc

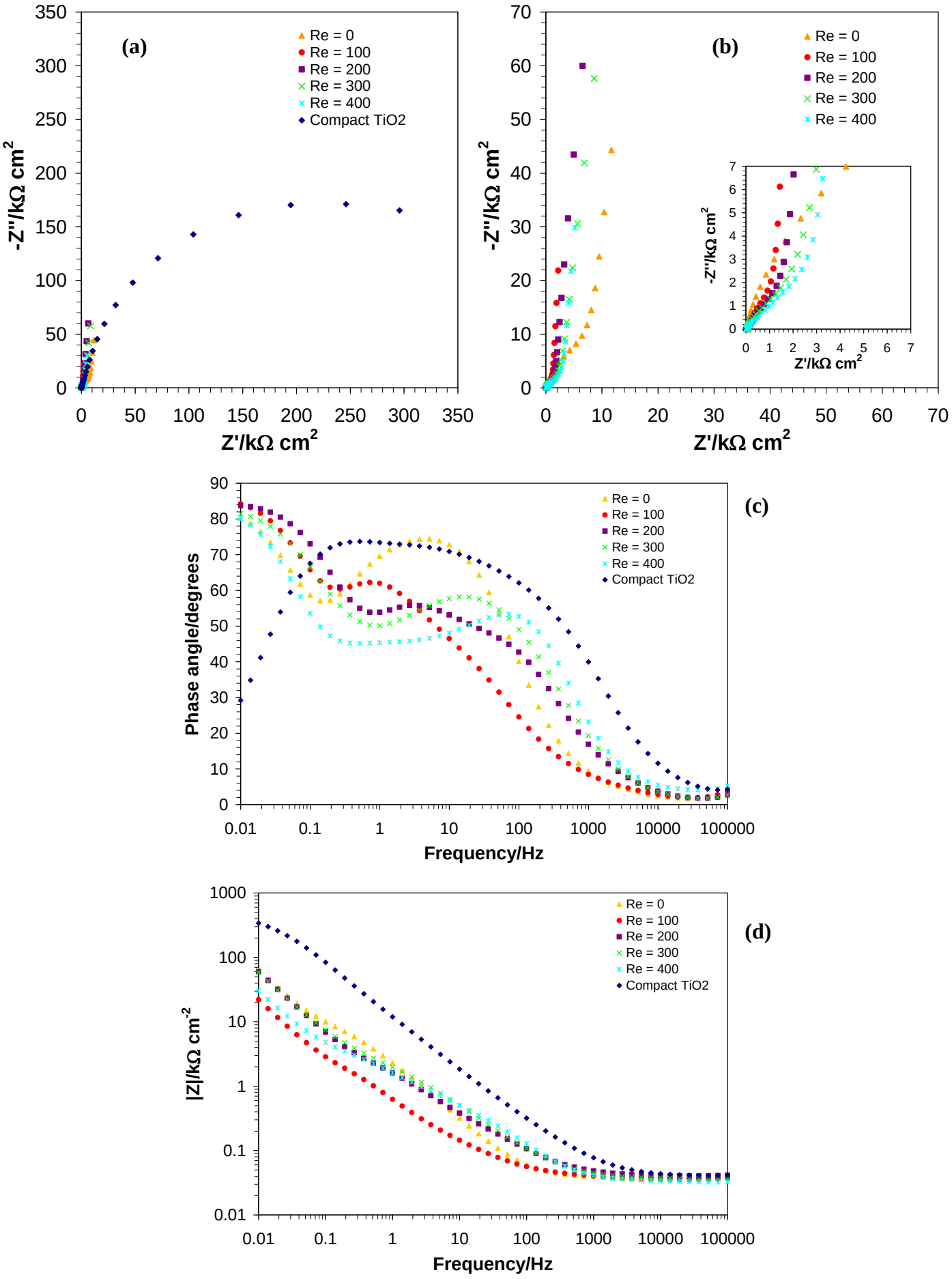

Figure 5

Click here to download Figure(s): Figure 5.doc

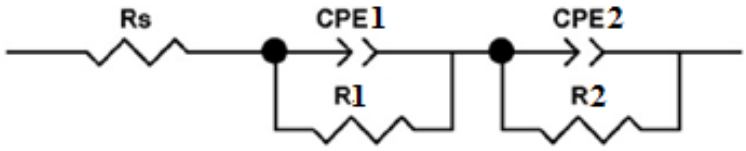

Figure 6

Click here to download Figure(s): Figure 6.doc

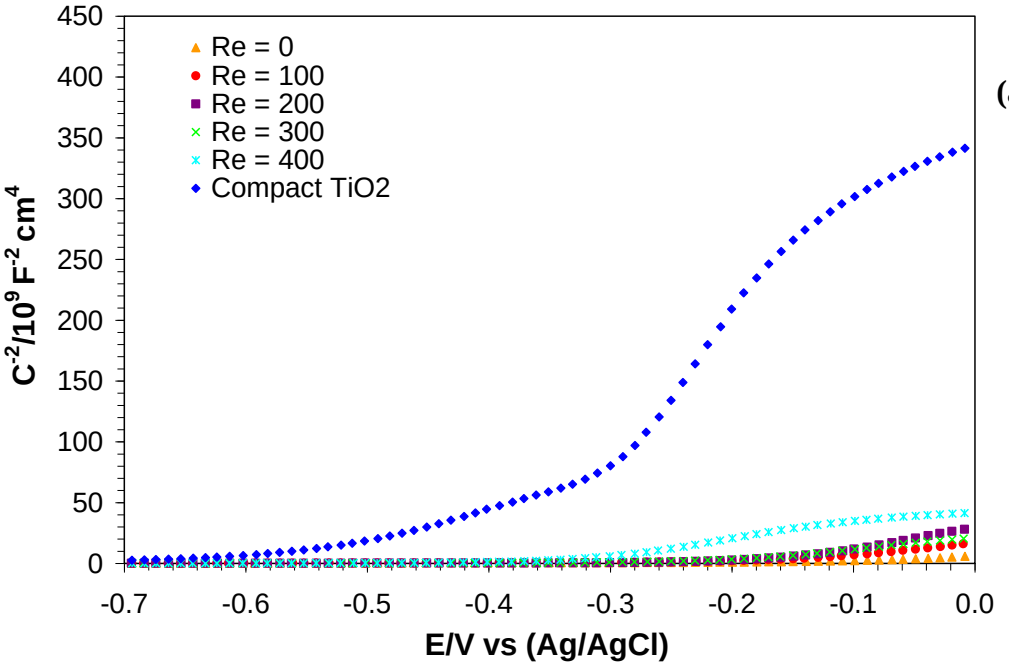

(a)

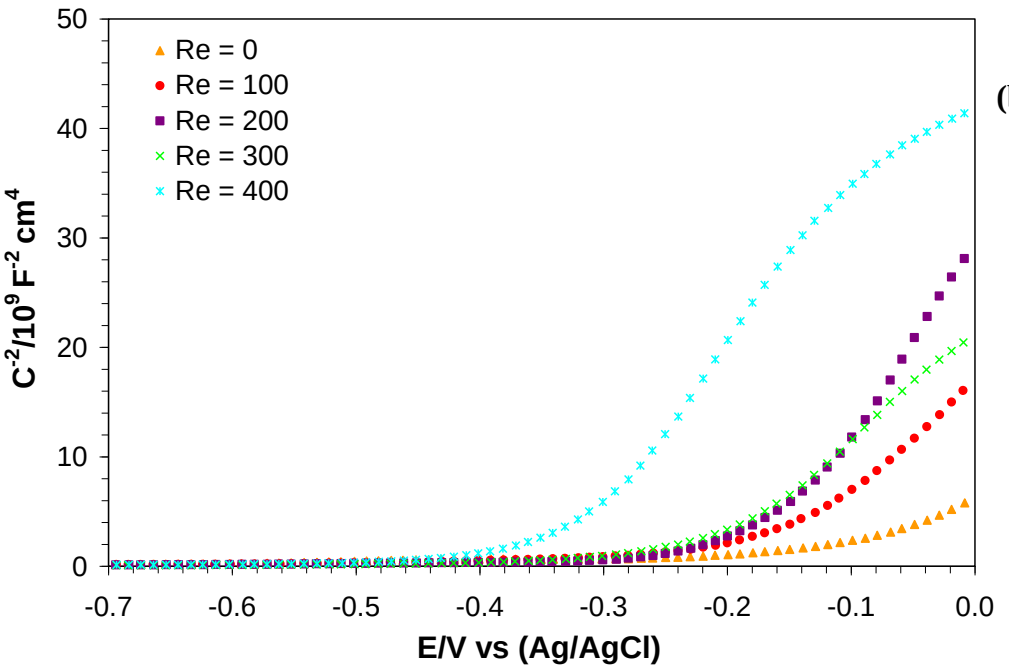

(b)

Figure 7

Click here to download Figure(s): Figure 7.doc

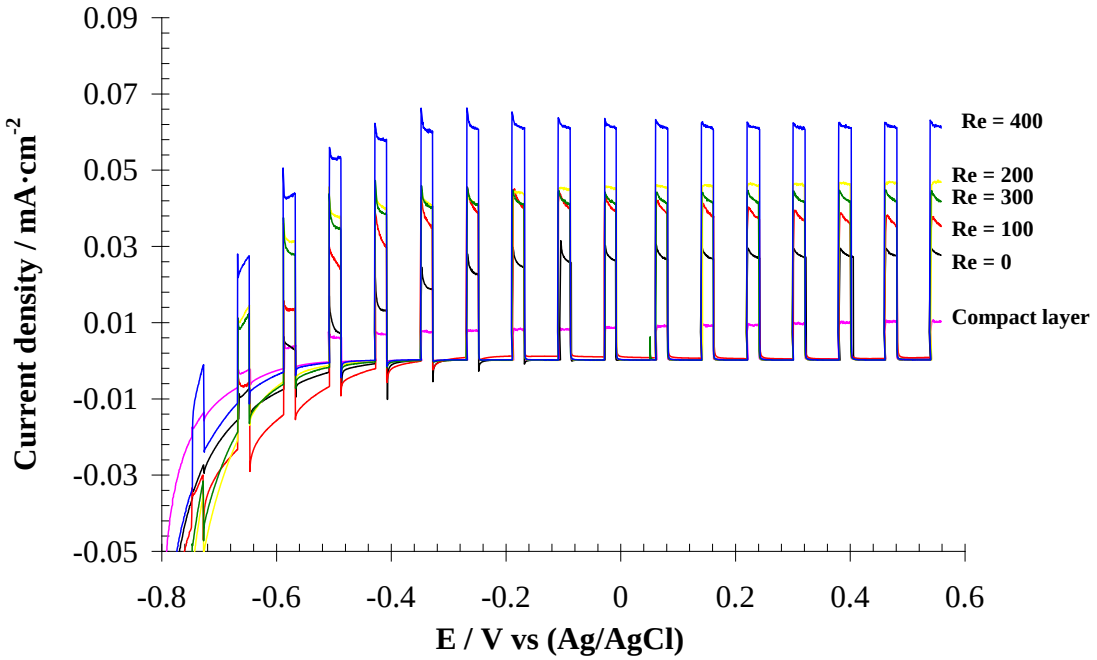

Figure 8

Click here to download Figure(s): Figure 8.doc

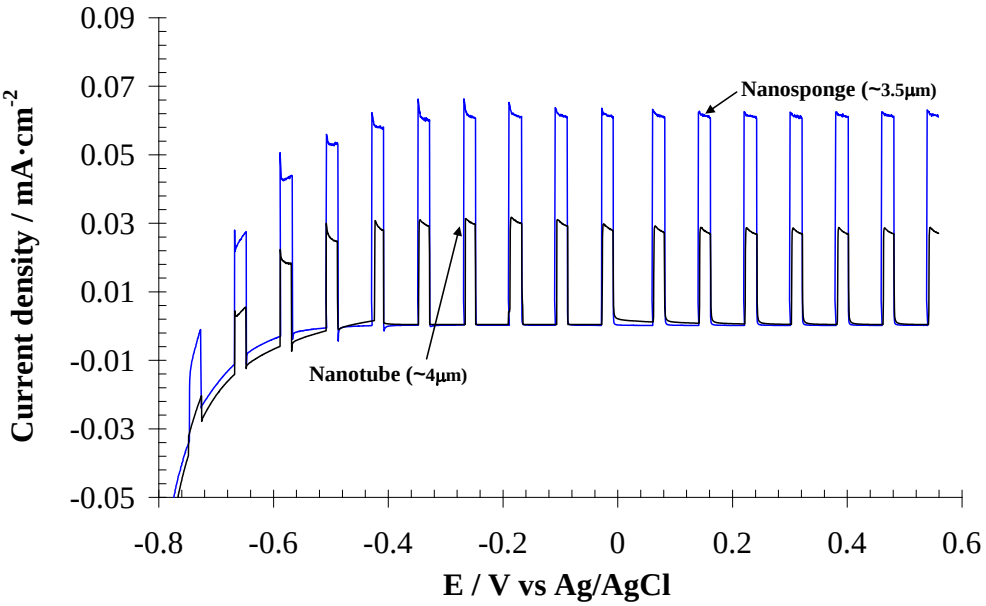

Figure 9

Click here to download Figure(s): Figure 9.doc